An Exploration of the Performance and Acoustic Characteristics of UAV-Scale Stacked Rotor Configurations

Siena K. S. Whiteside*, Nikolas S. Zawodny†, Xiaofan Fei‡, Nicole A. Pettingill§, Michael D. Patterson¶, and Paul M. Rothhaar‖
NASA Langley Research Center, Hampton, VA, 23681

As interest grows in rotor- and propeller-driven electric vertical takeoff and landing (eVTOL) aircraft for the Urban Air Mobility market, there is a potential for previously studied concepts to reemerge due to the opportunities afforded by novel technologies and operating modes. One such concept is the "stacked" rotor, which consists of multiple co-rotating rotors positioned co-axially with a small axial offset. The goal of the work presented in this paper is to determine whether stacked rotors offer a compelling advantage for eVTOL aircraft in terms of both performance and acoustic characteristics. Results are presented for new experimental tests and computational modeling of multiple stacked rotor configurations, and comparisons are made with conventional rotor configurations. Testing of thirteen separate configurations—each using the same blade shape—revealed a configuration that resulted in an increase in the rotor power loading efficiency by more than 7% and reduced noise by more than 3 dBA when compared with a conventional rotor with all blades located in the same rotational plane.

Nomenclature

A	=	Rotor disk area, πR^2 (m^2)
C_T	=	Thrust coefficient, $T/\rho A\Omega^2 R^2$
C_P	=	Power coefficient, $Q/\rho A\Omega^2 R^3$
L	=	Unweighted overall sound pressure level (dB)
L_A	=	A-weighted overall sound pressure level (dBA)
N_b	=	Number of blades per stacked rotor
P	=	Rotor mechanical power, ΩQ (W)
P^*	=	Density-corrected rotor mechanical power (W)
$p_{\text{meas.}}$	=	Measured ambient pressure (Pa)
Q	=	Rotor torque (N·m)
R	=	Rotor tip radius (mm)
T	=	Rotor thrust (N)
T^*	=	Density-corrected rotor thrust (N)
$t_{\text{meas.}}$	=	Measured ambient temperature (K)
$u_{P,b}$	=	Bias error in mechanical power (W)
$u_{Q,b}$	=	Bias error in torque (N·m)
$u_{T,b}$	=	Bias error in thrust (N)
$u_{r,\text{SPL}}$	=	Random sound pressure level uncertainty (dB)
ΔZ	=	Axial distance offset between stacked rotors (mm)
ϵ_r	=	Autospectral random uncertainty
θ	=	Elevation angle (deg.)
$\rho_{\text{meas.}}$	=	Measured ambient density (kg/m^3)
ρ_{SLSD}	=	Air density at sea level, standard day conditions (kg/m^3)
$\Delta\psi$	=	Azimuthal angle offset between stacked rotor blades (deg.)
Ω	=	Rotor rotation rate (rad/s, RPM)

*Aerospace Engineer, Aeronautics Systems Analysis Branch, 1 N. Dryden St. MS 442, AIAA Member.
†Research Aerospace Engineer, Aeroacoustics Branch, 2 N. Dryden St. MS 461, AIAA Member.
‡Pathways Intern, Aeronautics Systems Analysis Branch, 1 N. Dryden St. MS 442, AIAA Member.
§Research Aerospace Engineer, Aeroacoustics Branch, 2 N. Dryden St. MS 461, AIAA Member.
¶Aerospace Engineer, Aeronautics Systems Analysis Branch, 1 N. Dryden St. MS 442, AIAA Member.
‖Research Engineer, Dynamic Systems and Control Branch, 8 Langley Blvd. MS 308.

I. Introduction

Co-rotating, co-axially spaced rotors and propellers, hereby referred to as "stacked" rotors or propellers, have been explored multiple times throughout aviation history for a variety of reasons. For the purposes of this paper, the difference between a rotor and propeller is defined by the mode of operation: a rotor is operated predominantly in hover or edgewise flight, whereas a propeller is operated predominantly in axial forward flight. Figure 1 shows a notional stacked rotor consisting of two 3-bladed rotors and defines the variable conventions that will be used throughout this paper. The geometric parameters that characterize the stacked rotor concept, the relative azimuthal angle offset between upper and lower rotors, $\Delta\psi$, and the axial spacing between the planes of rotation, ΔZ, are seen most clearly in Figs. 1(b) and 1(c), respectively.

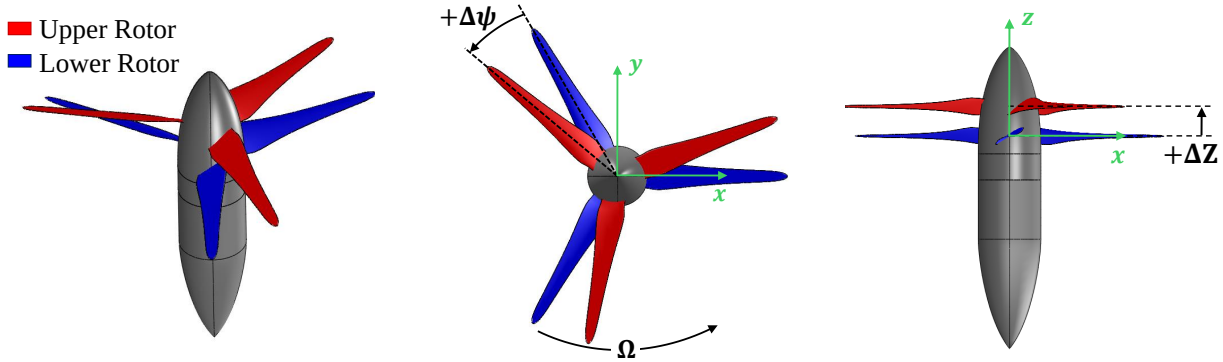

(a) Isometric view (b) Top View (c) Side View

Fig. 1 Notional stacked rotor consisting of two 3-bladed rotors. Configuration shown represents $\Delta Z/R = 0.15$ and $\Delta\psi = +20°$.

One of the first examples of the use of stacked propellers was in the 1940s for the XF5U-1 (nicknamed the "Flying Flapjack" or "Zimmer Skimmer"), shown in Fig. 2. The stacked prop-rotors on the XF5U-1 were a result of using two semi-rigid rotors, which were able to teeter to relieve high cyclic loads experienced during low speed, high angle of attack operation [1]. The stacked prop-rotor arrangement from the XF5U-1 was applied to the NASA Puffin concept, shown in Fig. 3, for the same reasons [2]. CFD studies and static sub-scale experiments of the Puffin's stacked prop-rotor system also showed additional benefits of 4% increased efficiency as well as a slight reduction in noise of < 1 dB when compared to a 4-bladed coplanar design, which were hypothesized to result from beneficial tip vortex interaction effects [3].

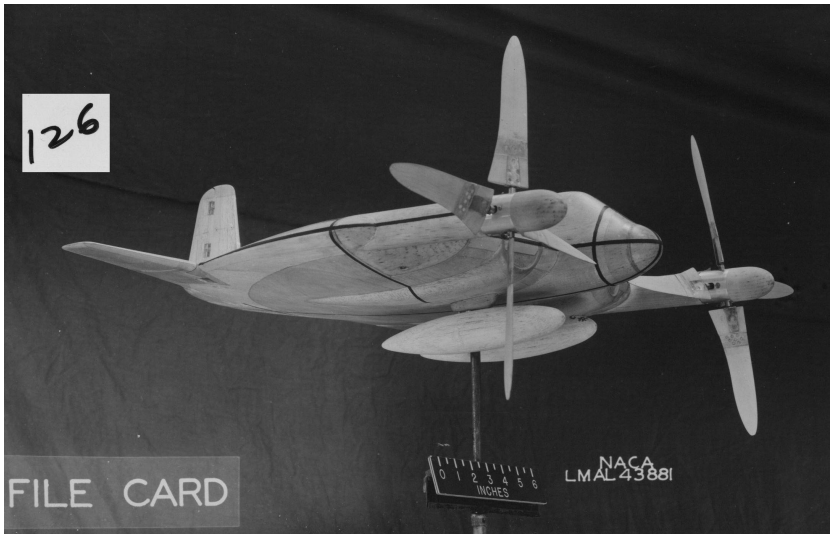

Fig. 2 XF5U-1 model from 1945 for the NASA Langley 20-foot spin tunnel [4].

Fig. 3 NASA Puffin aircraft concept with stacked prop-rotors.

Another instance of the stacked configuration is seen in the Hamilton Standard Variable Camber propeller developed and tested in the 1960s [5]. These stacked propellers incorporated two layers of variable pitch propellers that could be aligned to optimize performance for either static or cruise conditions. Extensive testing performed from 1964 to 1968 validated the ability to achieve increased static thrust; however, cruise efficiency was less than that of existing conventional propellers.

Stacked propellers were also proposed by Dobrzynski [6] in the early 1990s to obtain unequal blade spacing to reduce propeller noise in forward flight. Dobrzynski was not concerned with the stacked propeller concept per se, but a stacked configuration was advantageous for testing unequal azimuthal blade spacings because it overcame the challenge of balancing propellers with unequal spacing. Dobrzynski's studies focused on high subsonic to transonic Mach numbers and showed that noise could be reduced by approximately 4 dBA. For the configurations tested, he observed no significant changes in the aerodynamic performance of the stacked propellers relative to in-plane propellers with the same number of blades.

The Apache AH-64 tail rotor, developed in the early 1980s and still in use today, uses two unequally spaced 2-bladed teetering rotors. Unequal spacing was initially selected to improve mechanical clearance and was also found to reduce the 4 per revolution component of tail rotor noise [7]. In the 1990s, Rozhdestvensky investigated stacked rotors for use as tail rotors, referred to as "scissors rotors", through wind tunnel and flight tests [8]. Rozhdestvensky found improvements in rotor efficiency and found broadband noise benefits in flight.

In the last decade, there has been renewed interest in coaxial rotors for high speed rotorcraft. Uehara & Sirohi [9] found that stacked rotor performance was highly dependent on the relative azimuthal offset angle between rotors, and they found that a stacked rotor comprised of two 2-bladed rotors with an azimuthal offset angle of $+10^{\circ}$ outperformed its contra-rotating counterpart. In contrast, Ramasamy [10] tested a stacked 3-bladed rotor and found that a contra-rotating rotor gave better performance for all configurations tested. Bhagwat [11] compared Uehara & Sirohi's results with Ramasamy's results and used the U.S. Army's Rotorcraft Comprehensive Analysis System (RCAS) to gain insight into the aerodynamics of stacked rotors, hypothesizing that the main drivers of differences in performance are wake interactions and changes in the induced velocity seen by the top and bottom rotors.

Currently, there is a desire to find quieter and more efficient rotors and propellers for use in Urban Air Mobility (UAM) concepts. The goal of the research presented in this paper is to determine whether stacked rotors offer a compelling improvement in performance and noise during hover. A combined experimental testing and computational modeling campaign was conducted in which two primary geometric parameters associated with stacked rotors were varied: axial distance offset and azimuthal angle offset between rotors. Experimental aerodynamic and acoustic measurements were taken in a vented anechoic chamber, and a commercial surface vorticity flow solver was tested to determine its ability to replicate the aerodynamic measurements. This solver was also used to model Uehara & Sirohi's experiment in Ref. [9] to gain a better understanding of the capabilities of the solver and of the physics behind stacked rotors.

II. Experimental Testing

Experimental testing was performed to gain an understanding of the benefits which may be achievable through the use of stacked rotors and to generate experimental data to which computational results could be compared.

A. Technical Approach

1. Test Facility and Hardware

All testing was performed under static conditions in the NASA Langley Small Hover Anechoic Chamber (SHAC), formerly known as the Small Anechoic Jet Facility (SAJF). This facility measures 3.87 m × 2.56 m × 3.26 m (L × W × H) from wedge tip to wedge tip. Images of the test setup are provided in Fig. 4. As this figure shows, the facility has both an inlet and outlet (flow collector) to allow flow through the chamber, with the rotor support stand located at approximately the middle of the room in the lengthwise direction. A total of six B&K Type 4939 free-field microphones were used to acquire acoustic data across a range of elevation angles relative to the rotor plane, with microphone M3 located in the rotor plane. Details of the microphone locations in the SHAC facility are provided in Table 1. Since the microphone closest to the rotor, M3, is located at a radial distance of approximately twelve rotor radii from the hub, the SHAC microphones are considered to be in the acoustic far-field of the rotors tested in this study. A set of dual nylon screen meshes are positioned behind the rotor support stand for the purpose of delaying the onset of flow recirculation within the chamber [12]. These screens were positioned at respective downstream locations of five and nine rotor radii from the primary rotor plane and have respective open areas of 51% and 35%. Ambient room pressure, $p_{\text{meas.}}$, and temperature, $t_{\text{meas.}}$, were measured using a wall-mounted Mensor Type DPG 2400 pressure sensor and K-type thermocouple, respectively.

Table 1 Microphone Locations in SHAC Facility

Microphone	r (m)	θ (deg.)
M1	2.124	43.5
M2	2.102	26.5
M3	1.896	0.0
M4	2.004	-18.5
M5	2.273	-35.0
M6	2.286	-43.0

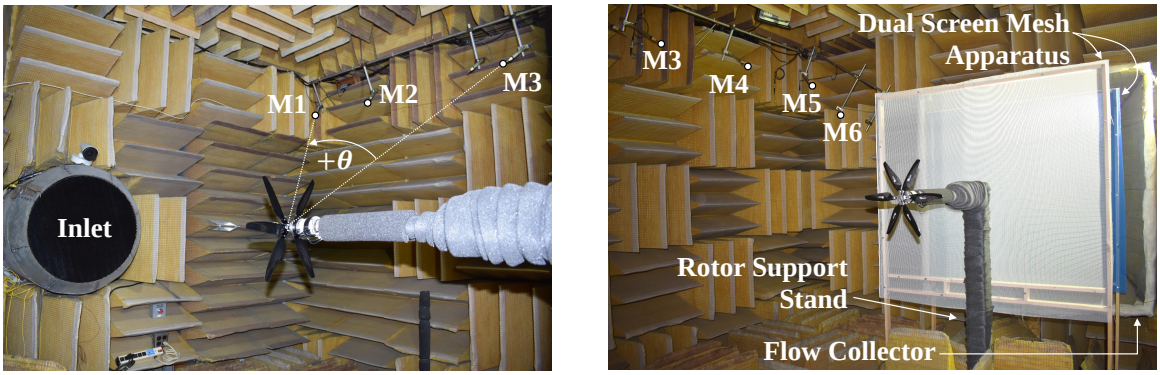

(a) Upstream view of SHAC facility

(b) Downstream view of SHAC facility

Fig. 4 Images of rotor test stand installed in SHAC facility.

Two sets of 3-bladed rotors (N_b = 3) were tested, each of which consists of the same KDE Direct 12.5x4.3 rotor blade set [13]. These rotors have a tip radius of R = 158.75 mm (6.25 in). The rotors are powered by a single brushless motor [14] to which they are affixed via a common motor shaft. The rotation rate of the motor was regulated using a Maytech^{TM} 40A-OPTO electronic speed controller (ESC), which in turn received pulse-width modulation commands from a Pololu Mini Maestro 12-channel USB servo controller. A 6-component AI-IA Mini40 multiaxis load cell is mounted behind the rotor-motor apparatus via a thermal isolator made out of acrylonitrile butadiene styrene (ABS) plastic. The load cell was used to measure steady and dynamic thrust and torque loads generated

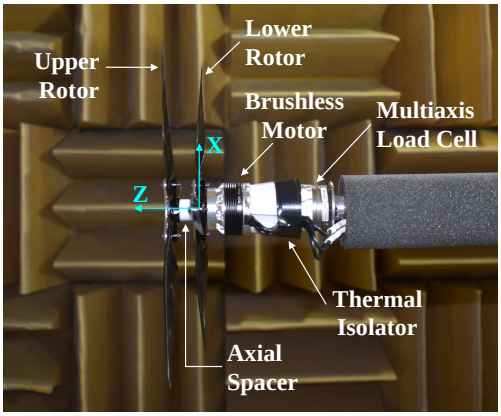

Fig. 5 Components of the tested rotor system.

by the various rotor configurations. Variations of axial (ΔZ) and azimuthal ($\Delta\psi$) offset between the two stacked rotors were achieved by using spacers with different mounting hole patterns. An annotated, close-up image of the rotor-motor system is provided in Fig. 5. Rotation rate of the rotor-motor system was monitored and measured using a non-intrusive laser sensor tachometer mounted in the floor of the facility. This sensor provided a transistor-transistor logic (TTL) pulse signal indicating each revolution of the motor housing.

2. Test Conditions

The experiments performed were intended to assess both the aerodynamic performance and acoustic characteristics of stacked rotor configurations in simulated hover conditions. The parameters that were varied in these tests were the axial offset (ΔZ) and the relative azimuthal offset ($\Delta\psi$) between rotor blade sets. The different test conditions are listed in Table 2.

Table 2 Stacked Rotor Geometric Test Conditions

↓ Parameter, Rotor Type →	Coplanar	Axial Offset	Azimuthal Offset
$\Delta Z/R$	0	0.08, 0.15, 0.20, 0.25	0.15
$\Delta\psi$	60°	60°	±10°, ±20°, ±30°, ±40°

As this table shows, a total of five different axial offset settings were tested for a symmetric azimuthal rotor condition of $\Delta\psi = 60°$. The case of $\Delta Z/R = 0$ warrants a special designation since this represents the baseline condition of a single, 6-bladed coplanar rotor. Furthermore, in addition to the symmetric case of $\Delta\psi = 60°$, eight different azimuthal offset conditions were tested for $\Delta Z/R = 0.15$. All rotor configurations were tested across a nominal rotation rate range of $3500 \leq \Omega \leq 6300$ RPM. This range was selected based on both the load range capabilities of the load cell and the flow recirculation characteristics of the SHAC facility.

3. Data Acquisition and Processing

Load cell and microphone data were acquired synchronously using National Instruments™ PXI-4472B dynamic signal acquisition modules installed in a PXI-1045 chassis. Data were acquired for individual rotor rotation rate conditions for a total acquisition time of ten seconds per condition at a sampling rate of 80 kHz. Each data run was initiated with a "ramp-up" of the motor to capture the transition of the rotor rotation rate to a steady-state condition. The onset of flow recirculation in the facility was diagnosed after the run was completed via visual interrogation of the acoustic spectrograms for that run. More specifically, the spectrograms for the out-of-plane microphones were interrogated because these are the ones most likely to display the effects of unsteady loading noise on the rotor blades. An example acoustic spectrogram with thrust and rotation rate time history for a representative data run is shown in Fig. 6. As Fig. 6(a) shows, the ramp-up of the motor occurs within the first 1.5 seconds of the data acquisition run, after which a steady rotation rate occurs starting at approximately 1.75 seconds. The acoustic spectrogram shows a fairly steady condition for a duration of approximately four seconds, as indicated by a consistent sound pressure level (SPL) at the third shaft harmonic of 265 Hz. At approximately six seconds into the data run, however, a considerable increase in acoustic energy is present in the sixth, ninth, and twelfth shaft harmonics. This increase in harmonic energy is associated with turbulent gusts recirculating within the facility and being ingested back into the rotor disk. Furthermore, additional fluctuations are visible in the thrust time history starting at approximately seven seconds. Therefore, calculation of a "clean" acoustic condition is performed by only considering the portion of the data run that starts with the achievement of a steady rotation rate condition and ends prior to the apparent onset of recirculation. This time duration is visually depicted by the darkened line plot in the thrust time history of Fig. 6(a). Figure 6(b) presents acoustic spectra for this same microphone (M5) for both the clean (pre-recirculation) subset of data and the spectra that includes the remainder of the data run (including recirculation). This spectral comparison clearly shows the dramatic increase in tonal energy at the previously mentioned shaft harmonics due to flow recirculation. Therefore, it is believed to be very important to isolate the pre-recirculation data in order to make fair acoustic comparisons between all of the tested rotor configurations. The time of onset for the recirculation effects mentioned previously was observed to be a function of the thrust generated by the rotor. Therefore, a common thrust condition was defined at which all rotor configurations would be compared with each other, ensuring both a common aerodynamic objective as well as a common amount of acoustic data between configurations. As with the case presented in Fig. 6, a thrust condition of $T \approx 9$ N (2 lb) was seen to provide a clean run duration of approximately four seconds. Acoustic spectra are then calculated using a Hanning window with 75% block

overlap with a 10 Hz frequency resolution. This results in an autospectral random uncertainty of $\epsilon_r = 11.1\%$, which translates to a random SPL uncertainty of $u_{r,\mathrm{SPL}} \approx \pm 0.51$ dB [15].

In addition to the calculation of narrowband acoustic spectra, periodic averaging was performed in order to differentiate between the deterministic and random components of the recorded signals [16, 17]. The TTL pulse signal from the laser sensor tachometer discussed previously was used to parse the acoustic time series data into blocks corresponding to individual revolutions of the rotor system, from which a mean rotor revolution time history was computed. This mean revolution time history was then subtracted from the individual time blocks, which were then processed as a random time series using a fast Fourier transform. This effectively yields a residual time history representative of the random fluctuating acoustic events present during the data run. Individual frequencies of interest (namely harmonics of the fundamental shaft rotation rate) were extracted in a similar periodic averaging manner, however, with the application of a narrow bandpass filter to the time series data prior to performing the previously mentioned periodic averaging. Specifically, a 2nd-order Butterworth narrow bandpass filter was applied to the time series data, with a ± 20 Hz frequency band centered around the frequency of interest. In this study, the extracted frequencies using this technique were limited to the first five blade passage frequency (BPF) harmonics, where the

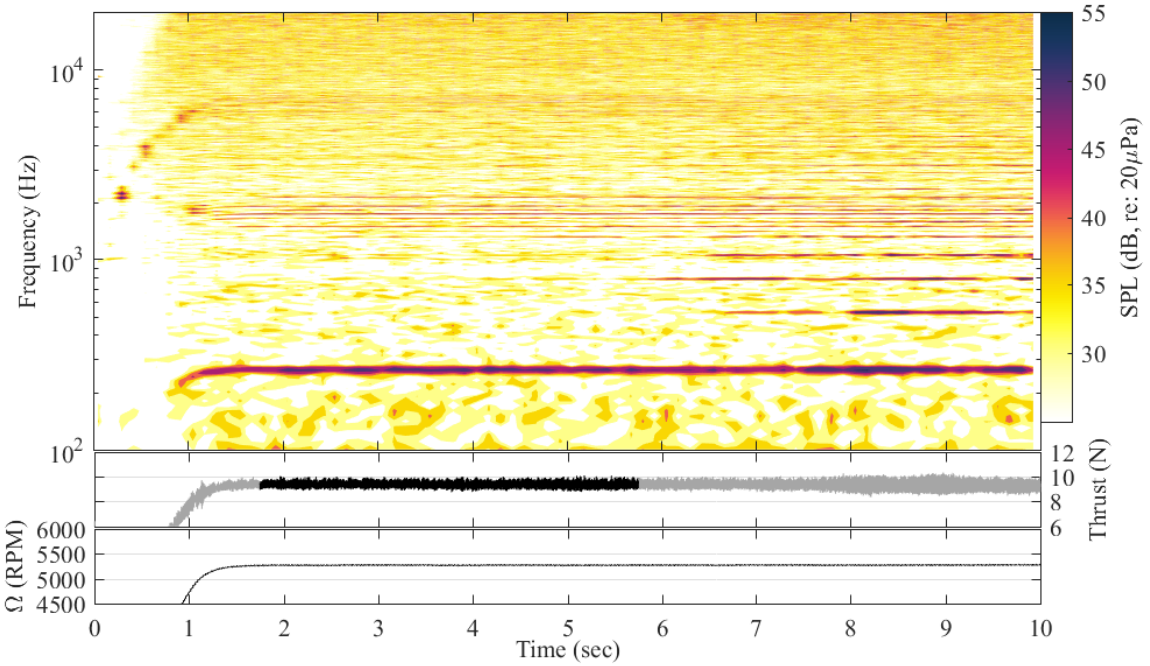

(a) Acoustic spectrogram (M5), thrust, and rotation rate, versus time

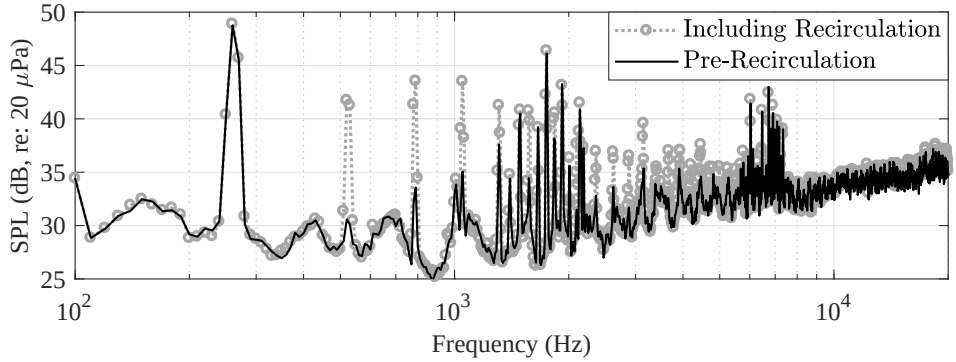

(b) Microphone M5 acoustic spectra before and after recirculation

Fig. 6 Effects of recirculation on rotor performance and acoustics. ***Note: case shown represents*** $\overline{\Omega}$ **= 5270 RPM,** $\Delta Z/R$ **=** ***0.15,*** $\Delta\psi = -40°$**.**

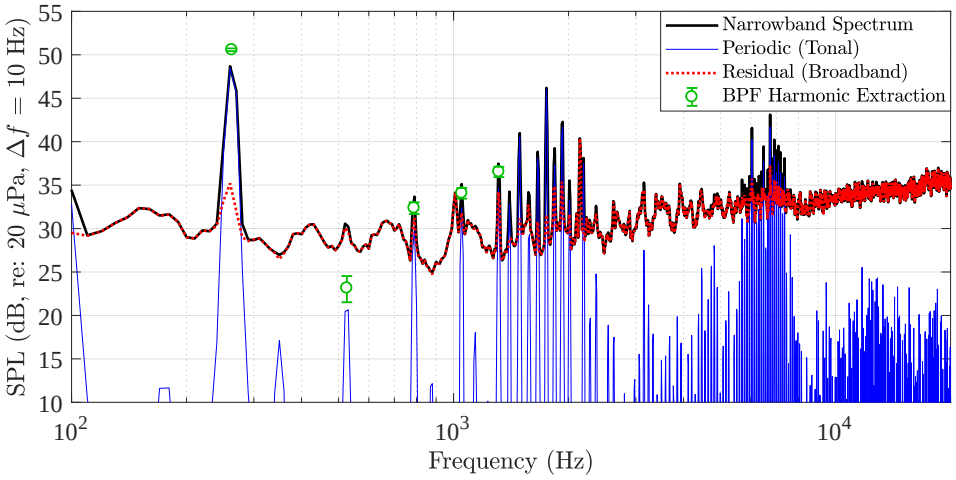

Fig. 7 Illustration of periodic and broadband noise extraction techniques applied to stacked rotor case shown in Fig. 6.

fundamental BPF is defined as N_b times the shaft rotation rate. As will be shown in the Results section, this frequency range was selected because it encompasses the most prominent rotor tones that do not coincide with noise evidenced to be due to the electric motor and/or test stand vibrations. An illustration of the different acoustic post-processing techniques applied to the stacked rotor case previously shown in Fig. 6 is provided in Fig. 7.

Uncertainties in the load cell measurements are presented in the following section in the form of error bars based on bias errors calculated in an in-situ manner. Specifically, the two load cell measurement components of primary interest (thrust and torque) were loaded with several known weights that encompassed the range of loads exhibited by the tested rotor configurations. The mean deviations of the measured loads as compared to the known values were then computed. The largest recorded deviation for each load component is treated as the worst-case bias error for each measurement. These bias errors were computed to be $u_{T,b} = \pm 0.107$ N for thrust and $u_{Q,b} = \pm 0.007$ N·m for torque. Quantification of bias errors for rotor mechanical power, P, were simply calculated according to $u_{P,b} = u_{Q,b} \times \partial P/\partial Q = u_{Q,b}\Omega$. Random errors in the load cell measurements are not accounted for in the following section. This is because the standard deviations in mean rotor loads computed on a per-revolution basis were found to be small compared to the bias error estimates.

B. Results

1. Performance Results

Figure 8 provides measured rotor thrust and torque profiles as a function of rotor rotation rate for the baseline, coplanar 6-bladed rotor configuration. Included with the measured data are 2nd-order polynomial curve fits of the data, each of which have a determination coefficient of $R^2 = 0.9999$. Although the aerodynamic loading profiles differ between the different stacked rotor configurations, very similar quality curve fits to the data were obtained. Assessment of the relative aerodynamic performance of the stacked rotors is done by comparing the dimensional power and thrust trends (P, T) between configurations. Although conventional rotor performance is based on the non-dimensional coefficients of C_T and C_P, these coefficients are typically obtained through experiments which use fixed rotor rotation rate with variable collective pitch, representative of the analyses carried out in Ref. [9]. However, the rotors tested in this study are fixed-pitch in nature and can only be controlled by varying rotation rate. Therefore, it is considered to be more

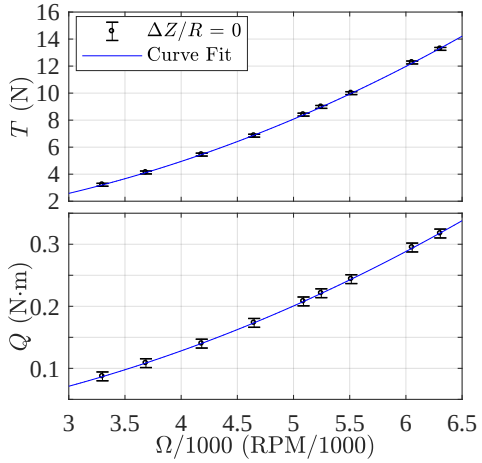

Fig. 8 Thrust and torque profiles as a function of rotation rate for coplanar rotor (ΔZ/R = 0).

appropriate to compare the dimensional power and thrust measurements for the rotor configurations tested in this study. Due to atmospheric variations throughout the duration of testing, however, the raw rotor performance data still need to be corrected to better relate the individual rotor configurations to each other. Therefore, the mean rotor power and thrust measurements are corrected by the ratio of the measured density and the density of air at sea level, standard day (SLSD) conditions:

$$[]^* = \frac{[]}{\rho_{\text{meas.}}} \times \rho_{\text{SLSD}}, \tag{1}$$

where $\rho_{\text{meas.}} = p_{\text{meas.}}/Rt_{\text{meas.}}$, $R = 287.058$ J/(kg·K) is the specific gas constant for dry air, and $\rho_{\text{SLSD}} = 1.225$ kg/m^3.

Figure 9 provides the power profiles of all stacked rotor configurations as a function of rotor thrust. Included with the data profiles are zoomed-in views of the upper two measured data points for better discernment of the trends between configurations. Figure 9(a) shows the power profile data for the cases of different axial offset between the stacked rotors, all for a common azimuthal offset angle of $\Delta\psi = 60°$. As this figure shows, there is a noticeable reduction in the overall rotor power profiles for the stacked rotor cases compared to the coplanar rotor ($\Delta Z/R = 0$). The cases of $\Delta Z/R = 0.15$ and $\Delta Z/R = 0.25$ yield the least required rotor power for the tested thrust conditions, with the former of these two cases performing slightly better. This result drove the decision to test azimuthally varying stacked rotor configurations at $\Delta Z/R = 0.15$. Figure 9(b) shows the power profiles for the cases of positive azimuthal offsets between rotors (upper rotor leading). As this figure shows, all of the tested cases with positive azimuthal offset yield slightly higher rotor power profiles compared to the baseline case of $\Delta\psi = 60°$. In contrast, the results of Fig. 9(c) show that the negative azimuthal offset case of $\Delta\psi = -40°$ yields a slight power trend reduction relative to the baseline case.

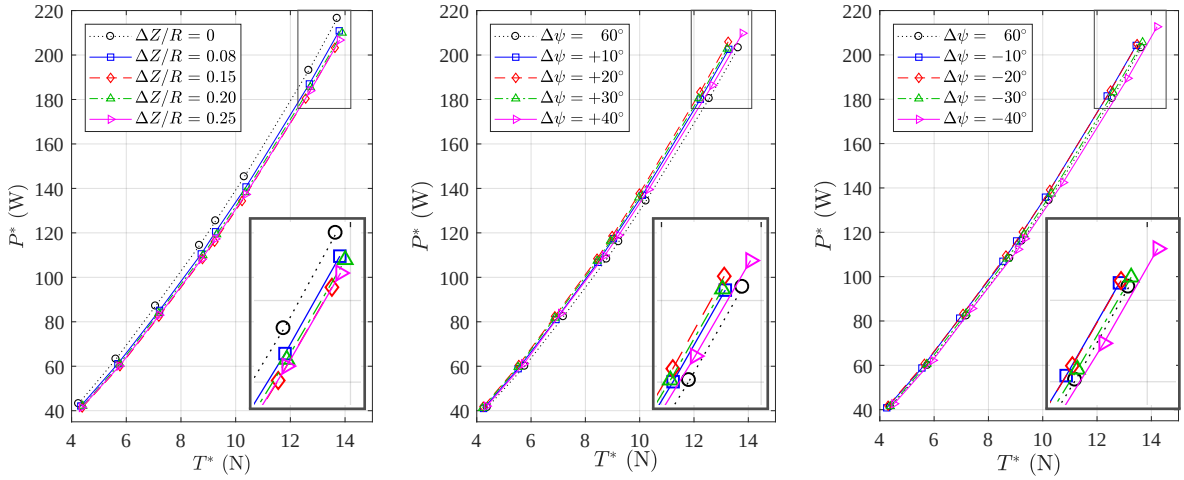

(a) Variation of axial offset for $\Delta\psi = 60°$ (b) Positive azimuthal offsets for $\Delta Z/R = 0.15$ (c) Negative azimuthal offsets for $\Delta Z/R = 0.15$

Fig. 9 Rotor mechanical power versus thrust trends for different stacked rotor configurations.

A final comparison of the baseline coplanar rotor, the symmetric rotor with axial offset $\Delta Z/R = 0.15$, and the azimuthally offset stacked rotor at $\Delta\psi = -40°$ is provided in terms of rotor power and power loading (T/P) as a function of rotor thrust in Fig. 10. In addition to the discrete measured data, 2nd-order polynomial curve fits to the P^* versus T^* data are also shown in Fig. 10(a). The three cases shown in this figure yielded $P^*(T^*)$ curve fit determination coefficients of $R^2 \geq 0.9999$. These curve fits were then used to compute the T^*/P^* curves shown in Fig. 10(b). As these figures show, there is a reduction in required power to achieve a desired thrust condition for the two stacked rotor cases compared to that for the baseline coplanar rotor. Although the bias uncertainties (indicated via error bars in Fig. 10(a)) promote ambiguity as to an exact performance benefit, the excellent curve fit profiles promote increased confidence when comparing the mean measured loads between configurations. At a common thrust condition of $T^* = 9.0$ N (2 lb) and using the curve fit profiles of P^* versus T^*, the stacked rotor cases of $\Delta Z/R = 0.15$ (symmetric) and $\Delta\psi = -40°$ yield rotor mechanical power savings of 6.9% and 7.6%, respectively, relative to the baseline coplanar case. These benefits decrease slightly to a respective saving of 5.3% and 6.7% for a common thrust condition of $T^* = 13.3$ N (3 lb). Similar reductions are computed on a power loading basis as well.

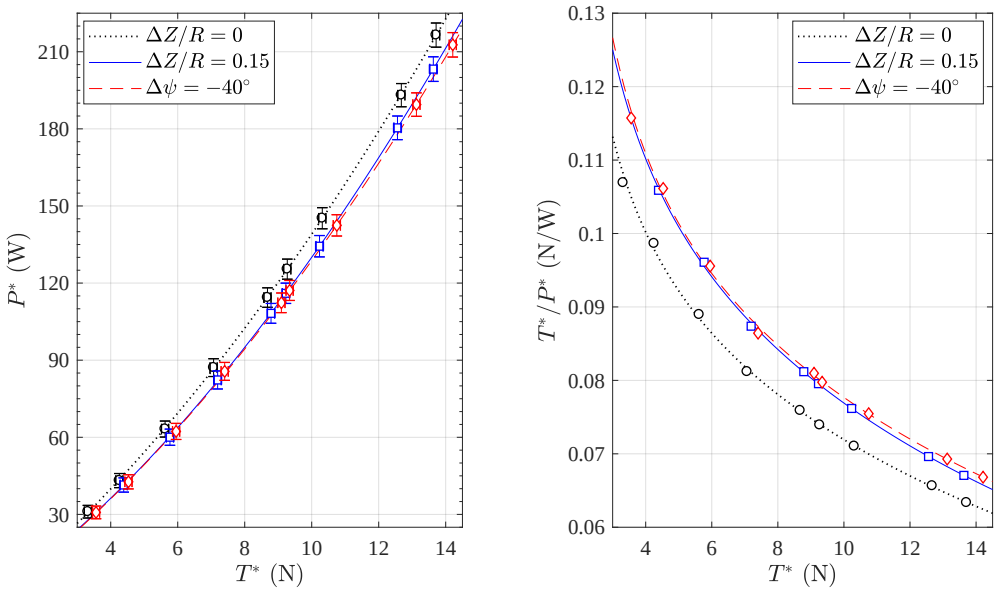

(a) Rotor Mechanical Power vs. Thrust

(b) Rotor Power Loading vs. Thrust

Fig. 10 Rotor power and power loading profiles as a function of thrust for baseline and select stacked rotor configurations. ***Note: symbols represent measured data, lines represent data from 2nd-order polynomial curve fits of measured P^* versus T^*.***

2. Acoustic Results

The acoustic characteristics of the different stacked rotor configurations are evaluated through comparisons of both overall sound pressure levels (OASPLs) and acoustic spectral content. Both unweighted and A-weighted OASPL sound metrics are considered (denoted as L and L_A, respectively) across a common frequency range of $100 \leq f \leq 20{,}000$ Hz. Figure 11 provides the measured unweighted OASPL partial directivity patterns for all tested stacked rotor configurations for a common thrust condition of $T^* \approx 9$ N (2 lb). One noteworthy trend in the directivities of Fig. 11(a) is how L increases out of the plane of the rotor. This is representative of the fact that broadband noise sources tend to be of highest amplitude out of the plane of the rotor [18]. This trend continues for the cases of stacked rotors with different azimuthal offsets in Figs. 11(c) and 11(b), with a slight change in behavior for the cases of $\Delta\psi = \pm 10°$. An explanation as to the causes of this change in directivity pattern is provided later in this section. It is interesting to

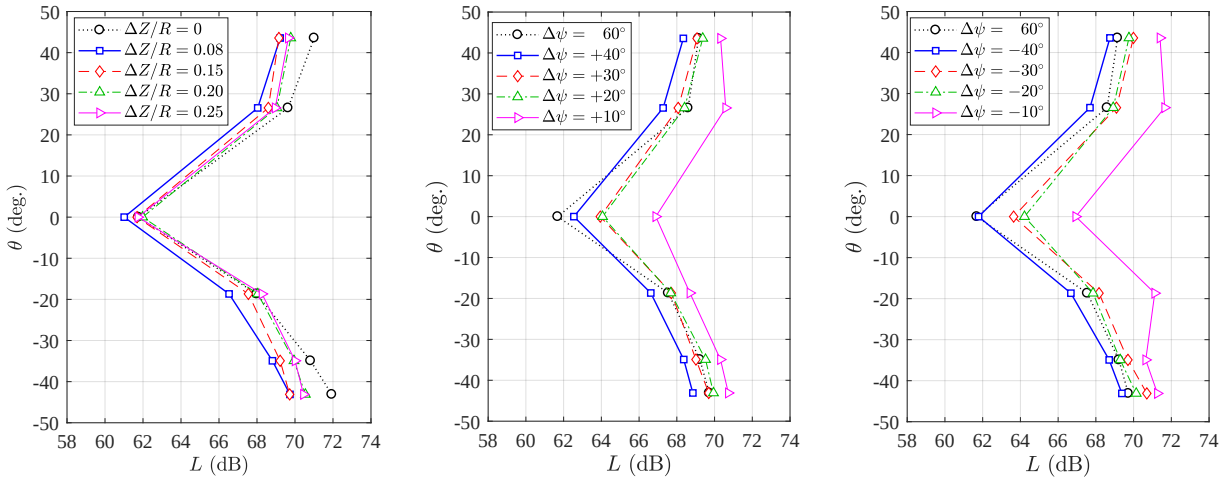

(a) Variation of axial offset for $\Delta\psi = 60°$

(b) Positive azimuthal offsets for $\Delta Z/R = 0.15$

(c) Negative azimuthal offsets for $\Delta Z/R = 0.15$

Fig. 11 Unweighted OASPL partial directivity comparisons between different stacked rotor cases for a common thrust condition of $T^* \approx 9$ N (2 lb).

note that the largest differences in OASPL occur at the farthest out-of-plane microphones for the cases of varying axial offset, although the in-plane microphone shows the largest OASPL differences for the cases of varying azimuthal offset. This provides evidence that the source of the OASPL differences for the stacked rotor cases of different axial offset are primarily due to changes in broadband noise sources, rather than steady thickness and loading noise sources.

To gain a clearer understanding of the relative roles of periodic and broadand noise for the stacked rotor cases of different axial offset, a subset of cases are selected for spectral interrogation in Fig. 12. This figure shows the narrowband acoustic spectra, extracted BPF harmonics, and extracted high-frequency broadband noise spectra at microphone M5 for the cases of $\Delta Z/R$ =0, 0.15, and 0.25. First considering the narrowband spectra in Fig. 12(a), it can be seen that there is a considerable amount of tonal content across a frequency range of $1.5 \leq f \leq 2.25$ kHz that approximately coincides with the acoustic spectra for an unloaded motor only case at the same rotation rate. Although the tonal amplitudes are considerably higher for the rotor cases, this is believed to be due to the torque exerted on the motor by the rotor blades changing the loading condition on and noise radiated by the motor. There is another region of prominent tonal content in the frequency range of $5.5 \leq f \leq 7$ kHz, which is also believed to be related to noise generated by the motor. The considerable spread in tonal frequencies for the rotor cases is believed to be related to eccentricities in both the rotational stage of the motor and in the rotor blades themselves. More information on the sources of this motor noise is provided in Refs. [19] and [20]. The presence of these prominent motor tones warrants a closer focus on the tonal content below 1.5 kHz, which is shown in Fig. 12(b) for these three rotor cases. It is worth noting that the coplanar rotor case ($\Delta Z/R = 0$) exhibits its highest tonal amplitudes at the sixth and twelfth shaft harmonics. This makes sense because the nominal BPF for this case would be $N_b = 6$ times the shaft rotation rate. The case of $\Delta Z/R = 0.15$, meanwhile, shows

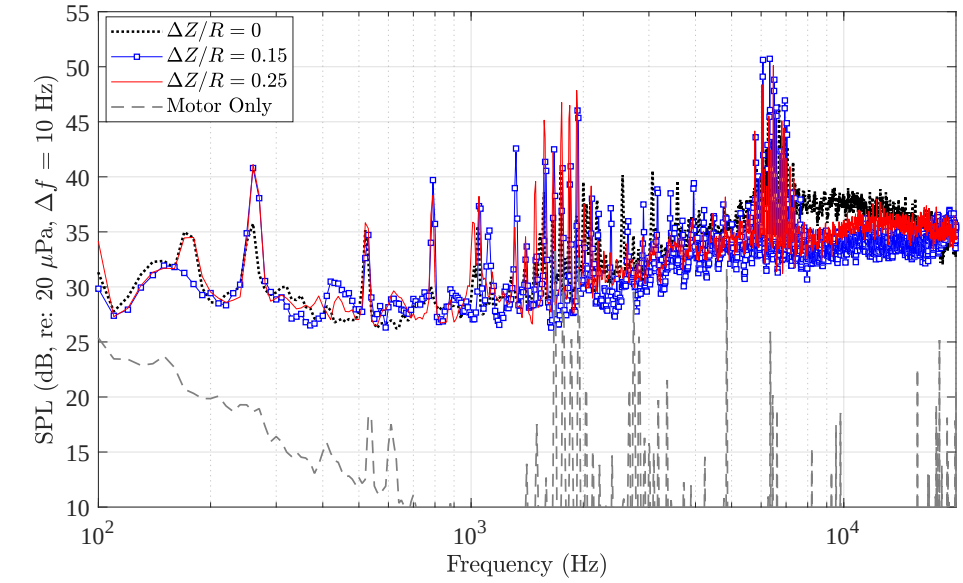

(a) Narrowband acoustic spectra

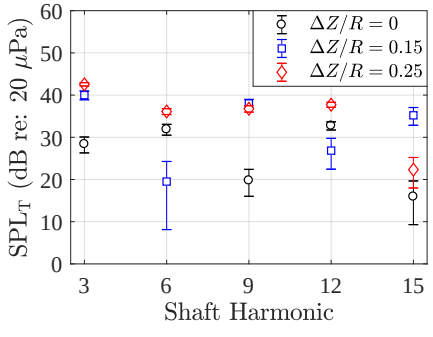

(b) Shaft order harmonics (tonal)

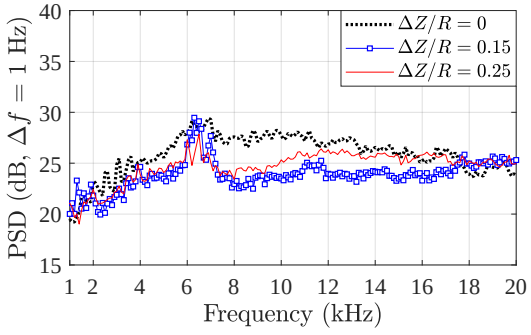

(c) High frequency acoustic spectral densities (broadband)

Fig. 12 Periodic and broadband spectral comparisons at microphone M5 between multiple axial offset configurations for a common thrust condition of T* ≈ 9 N (2 lb).

considerable amplitude increases in the third, ninth, and fifteenth shaft harmonics. This is presumably because they are more acoustically representative of two separate 3-bladed rotors of different aerodynamic loadings rather than one single 6-bladed rotor. The case of $\Delta Z/R = 0.25$ shows a further increase in the amplitude of the third shaft harmonic, as well as additional increases in the sixth and twelfth shaft harmonic amplitudes. Finally, Fig. 12(c) compares the extracted broadband spectra (see Fig. 7) for these three cases. The results show a considerable reduction in broadband noise across a frequency range of $7 \leq f \leq 18$ kHz for the case of $\Delta Z/R = 0.15$ as compared to the coplanar case. This broadband noise reduction is also evidenced to occur down to a frequency of 4 kHz; however, the retention of high-frequency motor noise in the broadband spectra make this difficult to quantify. The case of $\Delta Z/R = 0.25$ still shows a broadband noise reduction relative to the coplanar case at lower frequencies; however, at higher frequencies broadband noise increases compared to the $\Delta Z/R = 0.15$ case. Although the exact mechanism of this broadband noise reduction is currently unknown, it is believed to be due to the additional inflow velocity encountered by the lower stacked rotor due to the downwash of the upper rotor. This would result in reduced boundary layer thicknesses on the lower rotor blades, which effectively shift peak acoustic levels due to blade self noise to higher frequencies and lower amplitudes [21].

Figure 13 shows the narrowband acoustic spectra at microphone M5 for the cases of $\Delta\psi$ =-40°, -30°, and -10°, as well as the extracted BPF harmonics and extracted high-frequency broadband noise spectra for all negative azimuthal offset stacked rotor configurations. Note that these cases were selected for spectral interrogation because they represent a gradual increase in integrated levels as shown in Fig. 11. Furthermore, the cases with positive azimuthal offsets revealed very similar trends. Although the in-plane microphone (M3) showed the largest change in OASPLs across these

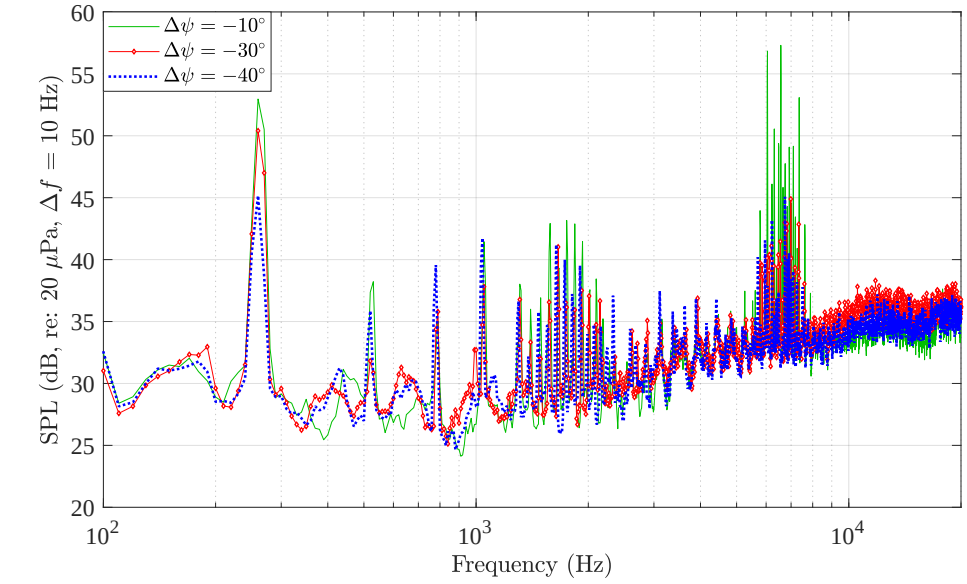

(a) Narrowband acoustic spectra

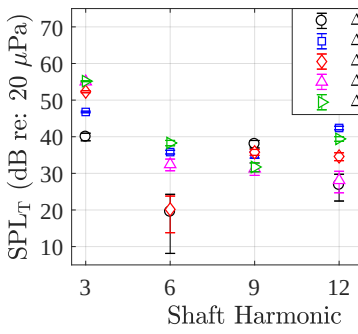

(b) Shaft order harmonics (tonal)

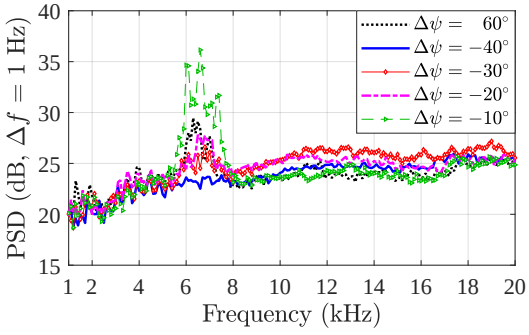

(c) High frequency acoustic spectral densities (broadband)

Fig. 13 Periodic and broadband spectral comparisons at microphone M5 between several azimuthal offset configurations for a common thrust condition of T* ≈ 9 N (2 lb).

configurations, M5 displays similar changes in tonal amplitudes while simultaneously displaying changes in broadband noise. The primary feature of interest in the narrowband acoustic spectra shown in Fig. 13(a) is the considerable increase in high-frequency motor noise for the $\Delta\psi = -10°$ case. Although the exact cause of this is unknown at this time, it is believed to be due to a test stand resonance condition unique to that rotor configuration. This increased tonal noise is partially responsible for the different OASPL directivity behaviors of the $\Delta\psi = \pm 10°$ cases relative to the other azimuthal offset conditions, as shown in Fig. 11. Despite this behavior, lower frequency tonal trends and higher frequency broadband trends can still be established. The shaft harmonic comparisons of Fig. 13(b) reveal a gradual increase in the BPF amplitude as a function of decreasing azimuthal offset. This is because reducing the relative azimuthal angle offset between the stacked rotor blades causes them to acoustically resemble two separate 3-bladed rotors. Presumably, further decreasing this azimuthal offset to $\Delta\psi = 0°$ would yield the highest BPF amplitude condition since this would be the most representative of two rotors in phase with one another. This would not be the actual behavior, however, since the loading noise generated by the two stacked rotors would be different than for two isolated rotors encountering the same inflow condition.

The extracted broadband spectra of Fig. 13(c) display a slight increase in broadband levels for the $\Delta\psi = -40°$ and $\Delta\psi = -30°$ cases relative to the $\Delta\psi = 60°$ case, which is then followed by a reduction for the $\Delta\psi = -20°$ and $\Delta\psi = -10°$ cases. Although the source of this oscillation in broadband noise behavior is currently unknown, it is believed to be related to relative wake and tip vortex convection and interaction effects between the two blade rows. Further investigation of this behavior is left for future work. Excluding the retained motor noise in the frequency range of $6 \leq f \leq 7.5$ kHz, the broadband noise levels of the $\Delta\psi = -10°$ case are nearly identical to those of the $\Delta\psi = 60°$ case. However, since the motor noise could not be fully removed in the periodic/broadband noise extraction process for all cases, it is still incorporated in the OASPL calculations. This is believed to be acceptable because the motor and support apparatus remain constant for all tested configurations and can be considered to be part of the noise-generating rotor system.

In Fig. 14, a final OASPL comparison is made between the 6-bladed coplanar rotor, symmetric axially offset stacked rotor at $\Delta Z/R = 0.15$, and azimuthally offset stacked rotor at $\Delta\psi = -40°$ for a common thrust case of $T^* \approx 9$ N (2 lb). These stacked rotor cases were selected because they were the ones shown in the previous section to be the most beneficial from a rotor power loading perspective. Interestingly, the case of $\Delta\psi = -40°$ represents the tested stacked rotor configuration that offers both the best performance gain and one of the largest acoustic reductions at this thrust condition. The unweighted and A-weighted OASPL partial directivity patterns in Figs. 14(a) and 14(b) show

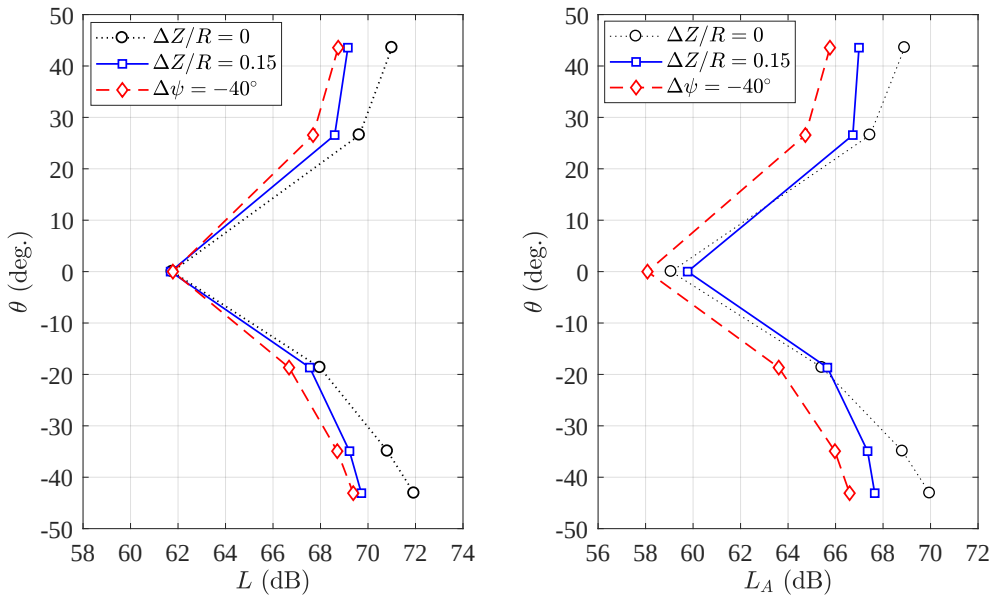

(a) Unweighted OASPL directivities

(b) A-weighted OASPL directivities

Fig. 14 Unweighted and A-weighted OASPL partial directivity comparisons between the 6-bladed coplanar rotor, symmetrically stacked rotor at $\Delta Z/R = 0.15$, and asymmetrically stacked rotor at $\Delta\psi = -40°$ for a common thrust condition of $T^* \approx 9$ N (2 lb).

similar trends, with the best integrated level reductions occurring out of the plane of the rotor. Specifically, the case of $\Delta\psi = -40°$ offers maximum unweighted and A-weighted OASPL reductions, relative to the baseline 6-bladed coplanar rotor case, of 2.5 dB and 3.4 dBA, respectively. These reductions occur at an elevation angle of $\theta = -43°$ (M6). It is important to note, however, that this overall noise reduction occurs at the expense of a slight increase in low frequency tonal harmonic energy, which is present in all of the stacked rotor configurations tested. This increase occurs because the presence of an axial offset between rotors results in different inflow and loading conditions on each blade row and inducing an azimuthal offset results in a non-ideal phasing between rotor blades. It is also important to note that the case of $\Delta\psi = -40°$ exhibits a reduction in high frequency motor tone amplitudes compared to the symmetrically stacked rotor at $\Delta Z/R = 0.15$. This reduction is largely responsible for the integrated level differences between these two cases in Fig. 14. Based on this observation, it is possible that the symmetrically stacked rotor could exhibit lower integrated levels if the motor-related noise sources are able to be either removed or effectively excluded.

III. Low-order Modeling of Stacked Rotors

The aim of the work presented in this section was to evaluate whether an existing commercial surface vorticity flow solver, FlightStream® [22], can be used to predict the performance of stacked rotors. Two experiments were replicated in FlightStream: the experiment described in Section II and an experiment conducted at UT Austin by Uehara & Sirohi [9].

A. Model Setup in FlightStream

The FlightStream predictions presented in the following sections were generated with FlightStream version 11.4 build 10122018a, and the simulation setup process is discussed here. Each stacked rotor was modeled using FlightStream's rotating reference frame method, in which the blades are fixed in space and the freestream is prescribed with an axial and angular velocity. Blade geometry was imported as a CAD model and re-meshed using FlightStream's trimmed mesher to achieve geometric fidelity which was comparable between the different rotors tested. The resulting meshes consisted of 3900 and 3400 faces per blade* for the KDE Direct 12.5x4.3 and UT Austin VR-12 rotors, respectively. The hub geometry was omitted. For visualization, an example of one of the KDE Direct 12.5x4.3 stacked rotor configurations as modeled in FlightStream is shown in Fig. 15.

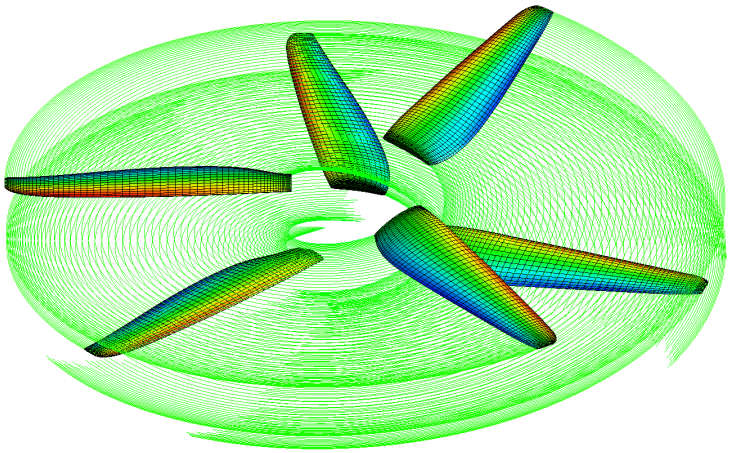

Fig. 15 Example of KDE Direct 12.5x4.3 stacked rotor with $\Delta\psi = -40°$ modeled in FlightStream. Wake trimmed short for clarity.

Treatment of the wake for each rotor geometry differed in the number of wake strands per blade as a result of differing blade aspect ratios (due to use of an isotropic mesh and roughly equivalent number of faces on each geometry), but was otherwise consistent. Each KDE Direct 12.5x4.3 blade shed 68 wake strands, whereas each UT Austin VR-12 blade shed 100. The Trefftz plane was set at twice the rotor diameter, and the wake refinement size was set at 200%. Relaxed and prescribed wake settings were found to produce similar trends during trial runs, so prescribed wakes were used for the predictions presented in this paper to reduce computation time. FlightStream's wake proximity avoidance

*The face counts given here are those of the geometric meshes. FlightStream's solver then applies a quad mesh filter that combines pairs of adjacent triangular faces into quadrilaterals in well-behaved regions, reducing the final face counts by about half.

feature was not suitable for the rotating reference frame method at the time of this study and was disabled. The lack of proximity avoidance allowed wake strands from the upper rotor to intersect the blades of the lower rotor, and although this did not lead to any convergence instability, it is a recognized limitation of this approach.

In FlightStream, the rotor wake is propagated by a constant uniform axial velocity set via the freestream velocity input. For rotors in hover, this freestream velocity should be set equal to the induced velocity experienced by the rotor. FlightStream calculates induced velocity as an area-average of the downwash velocity over annular discretizations after reaching a converged flow solution for the input freestream velocity[†]. Therefore, a fixed-point iteration scheme, initialized by an input freestream velocity guess and with a relaxation factor of 0.5, was used to converge upon the induced velocity value until the difference between the calculated induced velocity and input freestream velocity was less than 0.01 m/s.

FlightStream is capable of estimating viscous drag with either a laminar or turbulent boundary layer model. Testing with both boundary layer models showed that the turbulent boundary layer model significantly increased the torque but had little effect on thrust when compared to the laminar boundary layer model. Ultimately, the laminar model was selected due to a lack of boundary layer data from the experiments.

At the time of modeling, no exact KDE Direct 12.5x4.3 blade geometry was available. Instead, a scaled-down version of the T-Motor 15x5 carbon fiber rotor blade [23] geometry, with a 5° reduction in blade pitch angle, was used. This collective shallowing was determined by performing a trim calculation using the lifting rotor performance module of the ROTONET prediction code [24], based on a thrust-matching condition with the experimental data. The collective trim was found to vary by less than ±0.5° across the whole range of tested thrust (or rotation rate) conditions for this rotor. Therefore, although the scaled, pitched T-Motor 15x5 blade was found to be reasonably representative in thrust under the conditions tested in ROTONET, the lack of exact KDE Direct 12.5x4.3 blade geometry is likely to contribute some error to the FlightStream predictions.

B. KDE Direct 12.5x4.3 Rotor

Figures 16(a) and 16(b) show FlightStream predictions for thrust and power coefficient, respectively, versus axial offset compared with a subset of the experimental results for the KDE Direct 12.5x4.3 stacked rotor.[‡] Similarly, Figs. 17(a) and 17(b) illustrate trends versus azimuthal offset. FlightStream's predictions were found to be independent of rotation rate, suggesting that FlightStream's calculated induced velocity increased proportionally with rotation rate such that the blades' observed angle of attack and the wakes' propagation pitch remained constant. This trend is thought to be a fallout of the uniform induced velocity distribution prescribed by FlightStream's wake propagation scheme.

Overall, FlightStream seems to be able to capture *some* interaction effects between the stacked rotors, but predicted trends do not match those from the experiments. The primary reason for error is suspected to be the misrepresentation of the wake structure due to simplifications such as a uniform induced velocity distribution and a constant wake propagation rate. Since stacked rotors depend on the exploitation of blade-wake interactions, performance trends versus axial and azimuthal offset are likely highly sensitive to the exact placement and behavior of the upper rotor blades' wakes relative to the lower rotor blades.

[†]The FlightStream solver was set to run 50 iterations to achieve a converged flow solution.

[‡]The experimental data presented in Section II was acquired with slight variations in rotation rate (up to ±50 RPM from the average rotation rate at each target thrust condition). To most clearly show comparisons between the experimental results for each stacked rotor configuration, plots of density-corrected dimensional thrust versus power were used because variations in rotation rate would only result in tangential displacements along the trendline. In this section, thrust and power coefficients are plotted against geometric parameters for each target thrust condition. In this case, variations in thrust and power due to variations in rotation rate would cause significant distortions to the data representing a single target thrust condition. Therefore, C_T and C_P are used, which are normalized by both rotation rate and density and thus vary significantly less with rotation rate than dimensional thrust and torque.

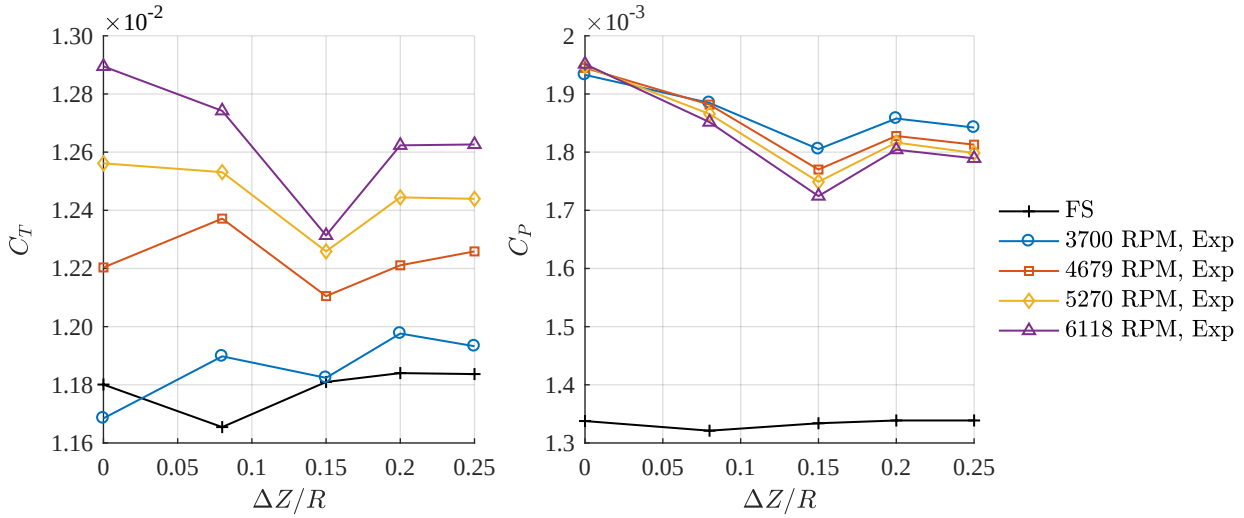

(a) Thrust coefficient vs. axial offset

(b) Power coefficient vs. axial offset

Fig. 16 Comparison of FlightStream and experimental thrust and power coefficients versus axial offset for KDE Direct 12.5x4.3 stacked rotor; $\Delta\psi$ = 60° for all cases.

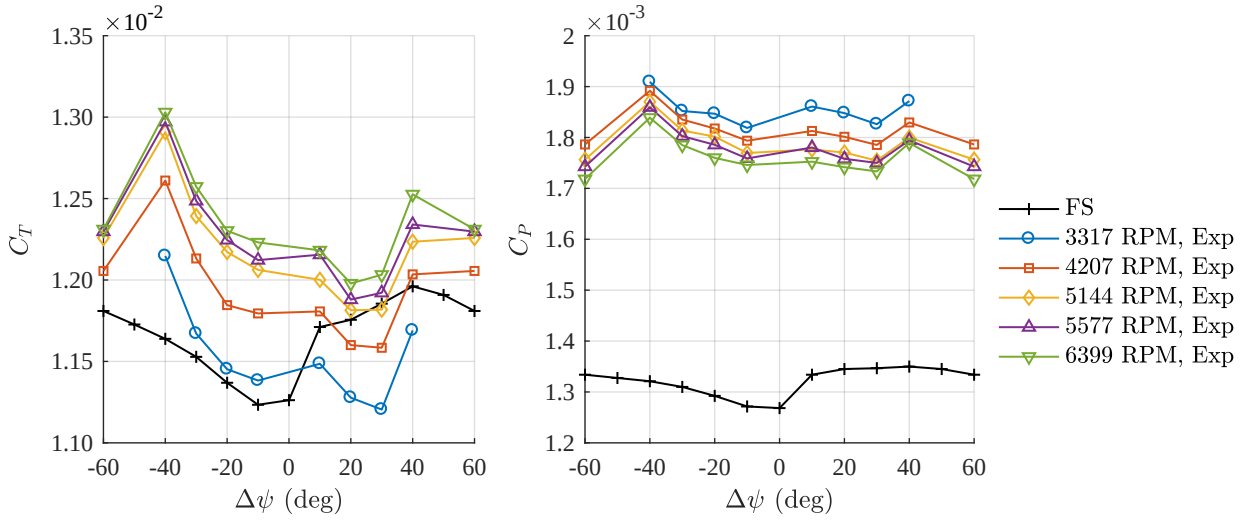

(a) Thrust coefficient vs. azimuthal offset

(b) Power coefficient vs. azimuthal offset

Fig. 17 Comparison of FlightStream and experimental thrust and power coefficients versus azimuthal offset for KDE Direct 12.5x4.3 stacked rotor; $\Delta Z/R$ = 0.15 for all cases.

C. UT Austin VR-12 Rotor

To better understand the causes for the discrepancy between FlightStream's predicted trends and those from the experiments, a simulation was performed of an experiment which yielded performance data for the individual upper and lower rotors. Uehara & Sirohi's [9] experiment at UT Austin tested a stacked rotor consisting of two 2.032 m diameter rotors with an axial offset equal to 13.8% of the radius. Each rotor featured two untwisted blades with a constant VR-12 airfoil cross section mounted to a rigid hub at a 3° pre-cone angle. The blades had a 0.080 m chord and a root cutout at 12% of the radius. The experiment was conducted at a constant rotation rate with upper and lower rotors held at the same constant torque; torque was kept constant by trimming the collective angle of the rotors. Azimuthal offsets of -50° to 50° were tested in 10° increments. In addition, one test was conducted with an azimuthal offset of 90°.

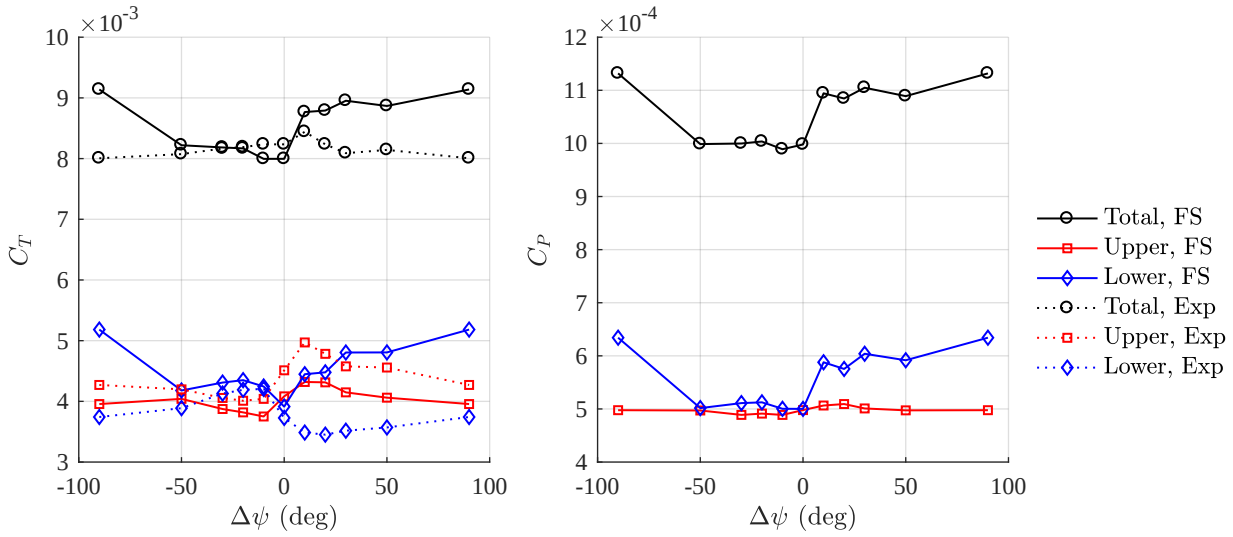

(a) Thrust coefficient vs. azimuthal offset

(b) Power coefficient vs. azimuthal offset

Fig. 18 FlightStream predictions for thrust and power coefficients versus azimuthal offset for the VR-12 rotor, compared with experimental thrust results.

Figure 18(a) compares the thrust coefficients predicted by FlightStream with Uehara & Sirohi's experimental results. It is interesting to note that the trends for the upper rotor match well across the entire range of azimuth offsets, but the trends for the lower rotor generally match only between -50° and 0°. FlightStream substantially over-predicts the lower rotor's thrust for azimuthal offsets between 10° and 90°, indicating that the induced velocity observed by the bottom blade is too low for these configurations. Predictions of power coefficient, shown in Fig. 18(b), support this conclusion. Experimental data is not shown in Fig. 18(b) as FlightStream's predicted magnitude of the power coefficient is incorrect; however, in the experiment power coefficients for the upper and lower rotors were kept equal and constant over the entire range of azimuthal offsets, and the same should be expected of the FlightStream predictions. Instead, FlightStream predictions show power coefficients to approximately match only in the -50° to 0° azimuthal offset region. Between 10° and 90°, the upper rotor's power coefficient essentially remains constant while the lower rotor consumes significantly more power.

Inspection of FlightStream's wake visualization, shown in Figs. 19 and 20, reveals that the presence of an axial offset subjects the lower rotor to two distinct operating regimes, depending on the azimuthal offset. Between -50° and -10°, the lower blades operate "above" the wake of the upper blades, and between 10° and approximately 110° (-70°), the lower blades operate "below" the wake of the upper blades. Transition occurs at approximately 0° and 120° (-60°) for this particular rotor design and operating condition. Combining these visualizations with the data in Fig. 18, it can be concluded that there must exist an azimuthally varying induced velocity distribution in the region immediately below the upper rotor. The upper rotor induces a locally higher axial or tangential velocity (or both) in the region below its wake, thereby decreasing the angle of attack observed by any blades present. Since FlightStream defines only one radially and azimuthally uniform induced velocity, it is unable to capture this detail, though the single induced velocity model appears adequate for the regime where the lower rotor operates above the upper rotor's wake.

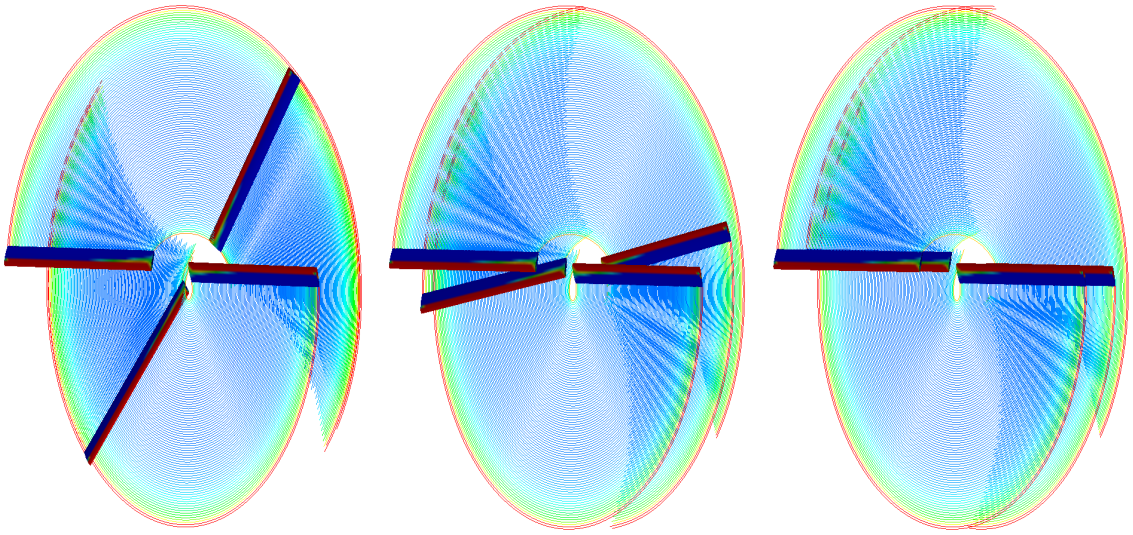

(a) $\Delta\psi = -50°$ (b) $\Delta\psi = -10°$ (c) $\Delta\psi = 0°$

Fig. 19 Wake visualization of VR-12 Rotor at various azimuthal offsets; wake strands trimmed short for clarity. In these images, the upper blades are the pair fixed in the horizontal position. For $\Delta\psi = -50°$ and $-10°$, the lower blades operate "above" the wake of the upper blades.

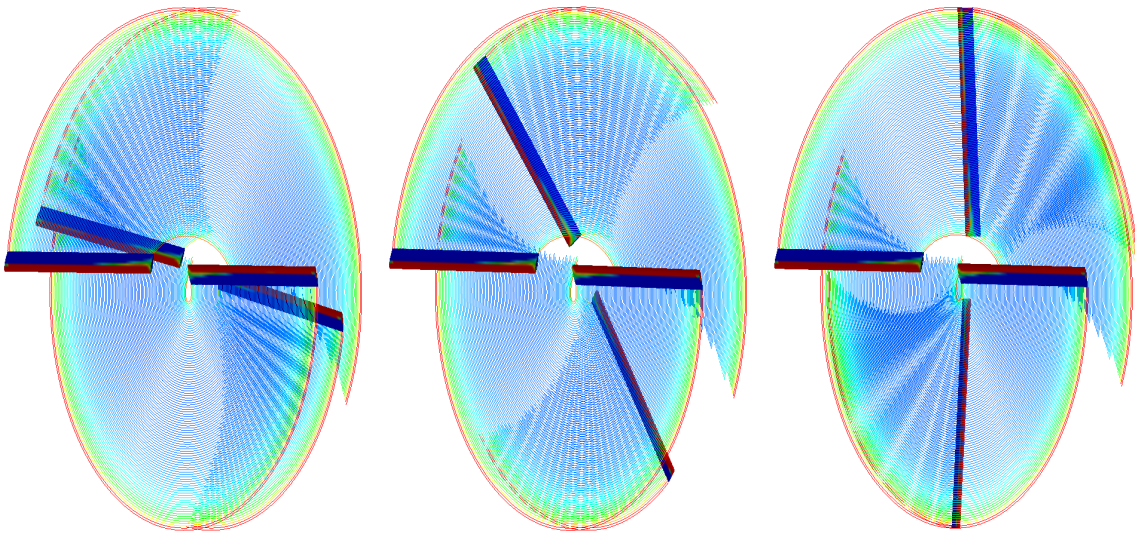

(a) $\Delta\psi = 10°$ (b) $\Delta\psi = 50°$ (c) $\Delta\psi = 90°$

Fig. 20 Wake visualization of VR-12 Rotor at various azimuthal offsets, continued. In these cases, the lower blades operate "below" the wake of the upper blades.

IV. Concluding Remarks and Future Work

This study investigated the aerodynamic performance and acoustic characteristics of stacked rotors of different axial distance offsets and azimuthal angle offsets under simulated hover conditions. Static experimental performance and acoustic measurements were acquired in a vented anechoic chamber, and a commercial surface vorticity flow solver was utilized to emulate the experimental stacked rotor configurations. The rotors tested experimentally in this study are fixed-pitch in nature and, therefore, are controllable only through variation of the rotor rotation rate. Although fixed-pitch rotors are operated in a different manner than those present on traditional rotorcraft, they are appealing to UAM markets due to their reductions in complexity and weight. This study conducted tests at small-UAV scale and found performance benefits similar to previous, larger-scale tests. Therefore, stacked rotors may be applicable to all sizes of UAM vehicles, provided that: (1) edgewise flight performance and acoustic characteristics are not worse than traditional rotors, and/or (2) stacked rotors can be used exclusively for vertical flight and effectively stopped and stowed for efficient forward flight.

Experimental thrust and torque measurements revealed an improvement in mechanical rotor power loading for several stacked rotor configurations. The configurations that performed the best relative to the baseline 6-bladed coplanar rotor are the symmetrically stacked rotor configuration with an axial separation distance of $\Delta Z/R = 0.15$ and the azimuthally offset stacked rotor at this same axial spacing and $\Delta\psi = -40^\circ$ (i.e., upper rotor lagging lower rotor by 40°). The respective nominal reductions in power required to achieve a common thrust of approximately 9 N (2 lb) were measured to be 6.9% and 7.6% relative to the baseline rotor case. Acoustic measurements revealed a very interesting trend in which the stacked rotor configurations yield gradual increases in low frequency tonal noise as functions of both increasing axial separation and decreasing azimuthal offset, as well as an oscillatory behavior in higher frequency broadband noise. Regardless of this oscillatory nature, all tested stacked rotor configurations yielded broadband noise measurements less than those of the baseline rotor. Maximum unweighted and A-weighted OASPL reductions compared to the baseline rotor of 2.6 dB and 3.4 dBA, respectively, were measured below the plane of the lower rotor at an observer angle of $\theta = -43^\circ$ (i.e., when the observer is 43 degrees below the plane of rotation) for the $\Delta\psi = -40^\circ$ case. This noise benefit decreases as the observer moves closer to an in-plane location ($\theta = 0^\circ$). This benefit is observed to be primarily due to a reduction in high-frequency broadband noise.

The surface vorticity method tested in this study was shown to be inadequate in its current state as a tool for the design of stacked rotors. Although conceptual-level estimates of thrust and torque can be produced, an improved induced velocity model is required before the performance of varying stacked configurations can be differentiated reliably. Specifically, the model must capture azimuthal variations in induced velocity in the region immediately below the upper rotor.

The tests conducted in this study revealed a stacked rotor configuration that offered both the best performance improvement and one of the largest acoustic reductions relative to a baseline 6-bladed coplanar rotor. It is important to note, however, that the common rotor blade geometries (such as blade radius, twist distribution, chord distribution) between upper and lower rotors as well as their fixed-pitch nature pose considerable limitations on the overall conclusions that can be drawn. It is believed that the reduction in broadband noise associated with the tested stacked rotors is due to a reduction in effective angles of attack on the lower rotor blades due to the increased inflow over these blades from the downwash of the upper rotor. This results in a reduced lower rotor blade trailing edge boundary layer thickness, thus yielding a reduction in airfoil self-noise. It is possible that incorporation of variable pitch capabilities (especially for the lower rotor) could further improve the observed performance; however, this will most likely counteract the observed noise reduction due to increased effective angles of attack and loading on the lower rotor blades. Future work will include high-fidelity CFD simulations of select cases to gain additional physical insight into the observed aerodynamic and acoustic behaviors. Simulations and experiments of select stacked rotors in edgewise forward flight will also be conducted to determine if the measured performance and acoustic benefits may be retained for flight conditions other than hover.

Acknowledgments

This work was performed under NASA Langley Research Center's Innovation Fund for Internal Research and Development.

References

[1] Lange, R. H., Cocke, B. W., Jr., and Proterra, A. J., "Langley Full-Scale Tunnel Investigation of a 1/3-Scale Model of the Chance Vought XF5U-1 Airplane," Tech. Rep. NACA-RM-L6I19, National Advisory Committee for Aeronautics, 1946. URL http://ntrs.nasa.gov/search.jsp?print=yes&R=20050019375.

[2] Moore, M. D., "NASA Puffin Electric Tailsitter VTOL Concept," *10th AIAA Aviation Technology, Integration, and Operations (ATIO) Conference*, Fort Worth, Texas, 2010. doi:10.2514/6.2010-9345, URL http://arc.aiaa.org/doi/abs/10.2514/6.2010-9345.

[3] Bain, J., "Acoustic Analysis of Single and Dual Plane Mejznik Propellers," Unpublished report, Georgia Tech Research Institute, 2010.

[4] NASA Langley GIS Team, "LMAL 43881," , 1945. URL https://crgis.ndc.nasa.gov/historic/File:V-173.jpg#file, accessed 26 Oct 2017.

[5] "Generalized Method of Variable Camber Propeller Performance Estimation," Internal Publication PDB 6408, Hamilton Standard, 1964.

[6] Dobrzynski, W., "Propeller Noise Reduction by Means of Unsymmetrical Blade-Spacing," *Journal of Sound and Vibration*, Vol. 163, No. 1, 1993, pp. 123–136.

[7] Amer, K. B., and Prouty, R. W., "Technology Advances in the AH-64 Apache Advanced Attack Helicopter," *29th Annual National Forum of the American Helicopter Society*, 1983.

[8] Rozhdestvensky, M. G., "Essential Results Obtained from Research Involved in Scissors Rotor," *21st European Rotorcraft Forum*, St. Petersburg, Russia, 1995.

[9] Uehara, D., and Sirohi, J., "Quantification of Swirl Recovery in a Coaxial Rotor System," *Proceedings of the 73rd Annual Forum*, AHS International, 2017.

[10] Ramasamy, M., "Hover Performance Measurements Toward Understanding Aerodynamic Interference in Coaxial, Tandem, and Tilt Rotors," *Journal of American Helicopter Society*, Vol. 6, No. 4, 2015, pp. 1–17.

[11] Bhagwat, M., "Co-rotating and Counter-rotating Coaxial Rotor Performance," *AHS Aeromechanics Design for Transformative Vertical Flight*, 2018.

[12] Stephenson, J. H., Weitsman, D., and Zawodny, N. S., "Mitigating the Pitfalls of Testing UAS Vehicles and Components in Anechoic Chambers," *176th Meeting of the Acoustical Society of America*, 2018.

[13] KDE Direct, "PROPELLER BLADES, 12.5" X 4.3, TRIPLE-EDITION SERIES (CW/CCW SET)," , 2018. URL https://www.kdedirect.com/products/kde-cf125-tp, accessed 01 Oct 2018.

[14] KDE Direct, "BRUSHLESS MOTOR FOR HEAVY-LIFT ELECTRIC MULTI-ROTOR (SUAS) SERIES," , 2018. URL https://www.kdedirect.com/collections/uas-multi-rotor-brushless-motors/products/kde4012xf-400, accessed 26 Oct 2018.

[15] Bendat, J. S., and Piersol, A. G., *Random Data Analysis and Measurement Procedures*, 3rd ed., John Wiley & Sons Inc., 2000, Chap. 6: Statistical Errors in Advanced Estimates, pp. 316–348.

[16] Zawodny, N. S., Boyd, D. D., Jr., and Burley, C. L., "Acoustic Characterization and Prediction of Representative, Small-Scale Rotary-Wing Unmanned Aircraft System Components," *AHS International 72nd Annual Forum*, 2016.

[17] Zawodny, N. S., and Boyd, D. D., Jr., "Investigation of Rotor-Airframe Interaction Noise Associated with Small-Scale Rotary-Wing Unmanned Aircraft Systems," *AHS International 73rd Annual Forum*, 2017.

[18] Brentner, K., and Farassat, F., "Modeling aerodynamically generated sound of helicopter rotors," *Progress in Aerospace Sciences*, Vol. 39, 2003, pp. 83–120. doi:10.1016/S0376-0421(02)00068-4, URL http://linkinghub.elsevier.com/retrieve/pii/S0376042102000684.

[19] Huff, D. L., and Henderson, B. S., "Electric Motor Noise from Small Quadcopters : Part I – Acoustic Measurements," *2018 AIAA/CEAS Aeroacoustics Conference*, AIAA, Atlanta, GA, 2018. doi:10.2514/6.2018-2952, aIAA Paper 2018-2952.

[20] Henderson, B. S., Huff, D., Cluts, J., and Ruggeri, C., "Electric Motor Noise from Small Quadcopters : Part II – Source Characteristics," *2018 AIAA/CEAS Aeroacoustics Conference*, AIAA, Atlanta, GA, 2018. doi:10.2514/6.2018-2953, aIAA Paper 2018-2953.

[21] Brooks, T., Pope, D. S., and Marcolini, M. A., *Airfoil Self-Noise and Prediction*, Hampton, VA, 1989. NASA RP 1218.

[22] Research in Flight, "FlightStream," , 2018. URL https://www.researchinflight.com/, accessed 10 October 2018.

[23] RobotShop, "T-Motor 15" x 5" Carbon Fiber Propeller Pair," , 2018. URL https://www.robotshop.com/en/t-motor-15-5-carbon-fiber-propeller-pair.html, accessed 27 Nov 2018.

[24] Weir, D. S., Jumper, S. J., Burley, C. L., and Golub, R. A., "Aircraft Noise Prediction Program Theoretical Manual Part 4: Rotorcraft System Noise Prediction System (ROTONET)," , 1995. NASA TM 83199.